



Gemstone nanoflower-shaped $\text{ZnIn}_2\text{S}_4/\text{CuS}$ heterojunction with ultralong lifetime of photoinduced carriers for photocatalytic hydrogen evolution

Ziqi Yu, Xue Luan, Han Xiao, Yupeng Yang, Di Luo, Jiangzhi Zi, Zichao Lian^{*}

School of Materials and Chemistry, University of Shanghai for Science and Technology, Shanghai 200093, P. R. China

ARTICLE INFO

Keywords:

Type-II-scheme mechanism
Photoinduced charge separation
Hydrogen evolution reaction
 $\text{ZnIn}_2\text{S}_4/\text{CuS}$ heterostructures
Ultralong lifetime

ABSTRACT

Efficient photoinduced charge separation achieving an extremely long lifetime for improving the photocatalytic activity in hydrogen evolution reaction (HER) is essential to obtain high performance. Here, we crafted and designed the gemstone nanoflower-shaped $\text{ZnIn}_2\text{S}_4/\text{CuS}$ (ZIS/CuS) heterostructure by the n-type ZIS nanoparticles grown on p-type CuS nanoflowers. The ZIS/CuS exhibited the photocatalytic HER rate of $1659 \mu\text{mol} \cdot \text{g}^{-1} \cdot \text{h}^{-1}$ under visible light irradiation which was higher than that of ZIS nanoflower and CuS gemstone-shape. It has been attributed to the formation of type-II-scheme p–n heterojunction structure with a strong interfacial built-in electric field and the efficient photoinduced charge separation up to an ultralong lifetime of 4.89 ms. It was directly demonstrated by the in-situ X-ray photoelectron spectroscopy and femtosecond-million second transient absorption spectra (fs-ms TAS). This study provides a new strategy for constructing type-II p–n heterostructures with high photocatalytic activity and strong stability for photocatalytic HER.

1. Introduction

With the development of mankind and the progress of civilization, energy problems and environmental pollution have become increasingly serious. Hydrogen is regarded as an ideal energy source in the future because of its high energy and pollution-free combustion. To regulate the sustainable development of energy in the environment, it is considered a feasible method to use a suitable photocatalyst to convert solar energy and decompose water into hydrogen without other pollution. It is of great significance to explore efficient and stable photocatalysts for hydrogen production to solve the problem of energy shortage and environmental pollution [1–7]. However, the low efficiency of photocatalytic hydrogen evolution reaction (HER) is the milestone to be conquered for achieving the practical application. The photogenerated carrier lifetime of semiconductors is extremely low due to the low photogenerated charge separation rate [8–12]. Many researchers devoted much effort to improving the photocatalytic efficiency in HER [13–25]. Therefore, the construction of the heterostructures with all-in-one multifunction to significantly decrease the unintentional recombination rates of the photoinduced electrons and holes was established for improving the photocatalytic performance in HER [26–29].

Particularly, ZnIn_2S_4 (ZIS) is a recently popular ternary layered

transition metal chalcogenide. Its band structure is adjustable with the bandgap around 2.06 ~ 2.85 eV and its conduction band in the position of the 1.20 eV [30,31], these characteristics indicate that its photo-generated electrons have strong reducing power, which is favorable for photocatalytic HER [32,33]. Generally, it can be considered feasible as an n-type semiconductor and has received increasing attention in recent years because of its excellent light stability, environmental friendliness, and special layered structure [34–38]. However, in practical applications, the rapid recombination of photogenerated electrons and holes showed that the photocatalytic activity of a single ZIS in HER was not high. To achieve high performance in HER, building heterogeneous structures with an efficient charge transfer pathway could provide a way to achieve multifunctionality in each phase. Particularly, copper sulfide (CuS) is inexpensive, has an adjustable band gap of 1.2 ~ 2.1 eV, and a non-toxic and suitable conduction band (CB), which can not only provide enough power to decompose and reduce water to produce hydrogen, at the same time, it is also a stable, economic and promising p-type semiconductor, which has a strong visible light absorption capacity [39–43]. The heterostructures formed by their coupling are very suitable for obtaining high photocatalytic activity in HER. Furthermore, for the type-II heterojunction with two semiconductors, theoretically, under light irradiation, electrons can transfer from catalyst 1 to catalyst 2 after the generation of electron-hole pairs, and the photogenerated

^{*} Corresponding author.

E-mail address: zichaolian@usst.edu.cn (Z. Lian).

<https://doi.org/10.1016/j.apcatb.2024.123702>

Received 6 December 2023; Received in revised form 2 January 2024; Accepted 4 January 2024

Available online 24 January 2024

0926-3373/© 2024 Elsevier B.V. All rights reserved.

holes can move in the opposite direction, thus realizing the spatial separation of photogenerated electron and holes [44,45]. Thus achieving significantly enhanced charge separation rates, ultralong lifetime of photoinduced carriers, and outstanding photocatalytic activity for HER are essential for constructing heterostructures [46,47].

Herein, the gemstone nanoflower-shaped $\text{ZnIn}_2\text{S}_4/\text{CuS}$ (ZIS) heterostructures were synthesized successfully by using the flower-like CuS as a seed. The photocatalytic HER rate ($1659 \mu\text{mol}\cdot\text{g}^{-1}\cdot\text{h}^{-1}$) of ZIS/CuS under visible light ($\lambda > 420 \text{ nm}$) is 3.34 times that of the original ZIS ($497.3 \mu\text{mol}\cdot\text{g}^{-1}\cdot\text{h}^{-1}$) and 26.3 times that of pure CuS ($63.02 \mu\text{mol}\cdot\text{g}^{-1}\cdot\text{h}^{-1}$), respectively. Furthermore, the ZIS/CuS has an apparent quantum yield (AQYs) of 4% at 400 nm with the highest activity in HER compared to current CuS-based and ZIS-based photocatalysts under visible light irradiation, listed in Tables S1 and S2. The high activity and excellent stability of ZIS/CuS were attributed to the efficient type-II-scheme mechanism and p–n heterojunction, which were directly demonstrated by the in-situ X-ray photoelectron spectroscopy (XPS) and femtosecond transient absorption experiments. Our work can pave a new route to designing the p–n heterojunctions with the effective photoinduced charge separation of the type-II-scheme for achieving high photocatalytic activity.

2. Experimental section

2.1. Materials

2.1.1. Synthetic processes of CuS

Sublimation S (2 mmol) and $\text{Cu}(\text{NO}_3)_2$ (1 mmol) were dissolved in ethanol (80 mL), and the mixture was stirred in a beaker for more than 30 min until the solution was a light blue solution. The mixture was transferred to a 100 mL reactor for reaction for 12 h at 120 °C. After the reaction, the product was mixed with ethanol and water, washed and purified, centrifuged twice, and finally dried under vacuum at 60 °C for further use.

2.1.2. Synthetic processes of ZIS

A 50 mL three-necked flask is used for synthesizing the ZIS. The glycerin (2 mL) is mixed with water (8 mL) solution ($\text{pH} = 2.5$) as a solvent, which dissolves ZnCl_2 (1 mmol), TAA (2 mmol), $\text{InCl}_3\cdot 4\text{H}_2\text{O}$ (2 mmol) until the solution becomes the transparent solution. The obtained mixture evenly was stirred for 10 min, and the solution was in a clear state. The flask was then placed in an oil bath for 2 h at a reaction temperature of 80 °C. After the reaction, it was washed and purified with deionized water and ethanol and then dried in a vacuum drying oven at 60 °C for 12 h.

2.1.3. Synthetic processes of ZIS/CuS

The prepared black powder CuS (10.0 mg) was dissolved in a 50 mL three-mouth flask in a mixture of water (8 mL) and glycerin (2 mL) ($\text{pH}=2.5$). After stirring for 30 min, it was added to the mixture of the TAA (2 mmol) ZnCl_2 (1 mmol), and $\text{InCl}_3\cdot 4\text{H}_2\text{O}$ (2 mmol) into the flask successively. The obtained suspension was heated in the oil bath for 2 h under magnetic stirring at a reaction temperature of 80 °C. After the reaction, the product was washed with deionized water and ethanol, and then the solid product was vacuum dried at 60 °C for 12 h. We also synthesized different ZIS/CuS using different amounts of CuS (6.0, 8.0, 12.0 mg).

2.2. Characterizations

The morphologies of samples were recorded through TEM (FEI Tecnai G2 F20, USA) and FESEM (Hitachi SU8010 system). The EDS elements mapping was analyzed using a JEOL JEM-2100F transmission electron microscope. UV–vis absorption spectra were obtained using a 1900i spectrophotometer (Shimadzu, Japan). Inductively coupled plasma emission spectroscopy (ICPOES, Agilent 5110) was used to

determine the Zn, Cu, and In mass ratios of the samples, respectively. X-ray photoelectron spectroscopy (XPS) measurements using a 300 W Al $K\alpha$ radiation source were performed on a Thermo K-Alpha spectrometer, with the binding energy carbon ($\text{C}1\text{s} = 284.6 \text{ eV}$) as the reference for the calibration. The TriStar II 3020 system (Micromeritics Instrument Corp.) was used to measure the BET surface area and pore size distribution of the samples.

2.3. Photocatalytic water hydrogen evolution

To measure the photocatalytic water hydrogen evolution reaction (HER), the amount of hydrogen evolution in the samples was detected by gas chromatography-2014 (Shimadzu, Kyoto, Japan) and the nitrogen is used as a carrier gas. The reaction was carried out by adding 3 mL of ultrapure water and 5.0 mg of sample with sacrifice agent (0.35 M Na_2SO_3 and 0.25 M $\text{Na}_2\text{S}\cdot 9\text{H}_2\text{O}$) to a 25 mL quartz photoreactor and stirring well by ultrasonication. We then vacuumed the reactor several times with nitrogen cycles until the air and solutes were completely removed, followed by irradiation. The light source was a 300 W xenon lamp (CEL-HXF300, Beijing China Education Au-light Technology Co., Ltd.), with a UV cutoff filter ($\lambda > 420 \text{ nm}$), and placed 6 cm away from the reactor. Using different single-wavelength filter, the apparent quantum efficiency (AQY) was measured [48]. Light intensity was measured using a light radiation instrument (CEL-NP2000–2). The calculation formula of AQY is shown below:

$$\begin{aligned} \text{AQY} &= \frac{\text{number of reacted electrons}}{\text{number of incident photons}} \times 100\% \\ &= \frac{\text{number of evolved } \text{H}_2 \text{ molecules}}{\text{number of incident photons}} \times 100\% \end{aligned} \quad (1)$$

2.4. Photoelectrochemical (PEC) measurements

All PEC measurements were performed using an electrochemical workstation (CHI-660E) with a conventional three-electrode system. The 0.5 M Na_2SO_4 aqueous solution ($\text{pH} = 6.8$) was used as the electrolyte. Perfluoro sulfonate polymer solution (10 μL , 5%), ethanol (500 μL), and photocatalyst (3.0 mg) were mixed to obtain the solution, the above 150 μL solution was dropped onto a fluorine-doped tin dioxide (FTO) conductive glass of $A = 1 \text{ cm}^2$. The above samples need to be vacuum-dried at 60 °C for 1 h to get the working electrode. The platinum sheet electrode was used as the counter electrode and the silver chloride electrode (Ag/AgCl) as the reference electrode for the PEC measurements. Under visible light irradiation, the photocurrent density of the samples was measured at 0.5 V voltage by an electrochemical workstation. A 300 W Xenon lamp with a UV filter ($\lambda > 420 \text{ nm}$) about 6 cm in front of the photoreactor as a visible light source. The electrochemical impedance tests were performed with open circuit voltages in the frequency range of 10^5 to 0.01 Hz and an AC voltage of 5 mV. Mott-Schottky plots to determine the flat potential were obtained at three different frequencies, which were performed in 0.5 M Na_2SO_4 using a standard three-electrode cell with a Pt foil as the counter electrode, Ag/AgCl as the reference electrode, and the photoanodes as the working electrode, respectively [49,50]. The potential vs. NHE (normal hydrogen electrode) was calculated using the following formula (2):

$$E_{\text{vs-NHE}} = E_{\text{vs-Ag/AgCl}} + 0.1976 + 0.0592 \times \text{pH} \quad (2)$$

3. Results and discussion

3.1. Structural characterization

The procedures of synthesizing gemstone nanoflower-shaped ZIS/CuS were shown in Fig. S1, in which the CuS nanoflower (Fig. S2a) was

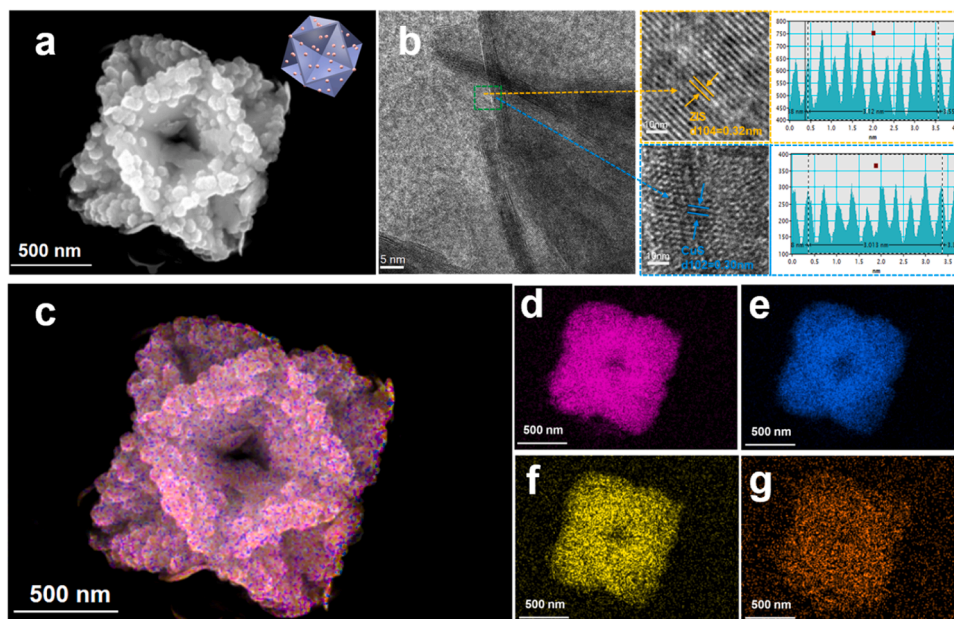


Fig. 1. (a) Representative FESEM image of individual ZIS/CuS, the cartoon picture of ZIS/CuS displayed in the top right corner. (b) The HRTEM image of ZIS/CuS. (c) The merged EDS-mapping image of a single ZIS/CuS. (d-g) The elements of the S, Cu, Zn, and In, respectively.

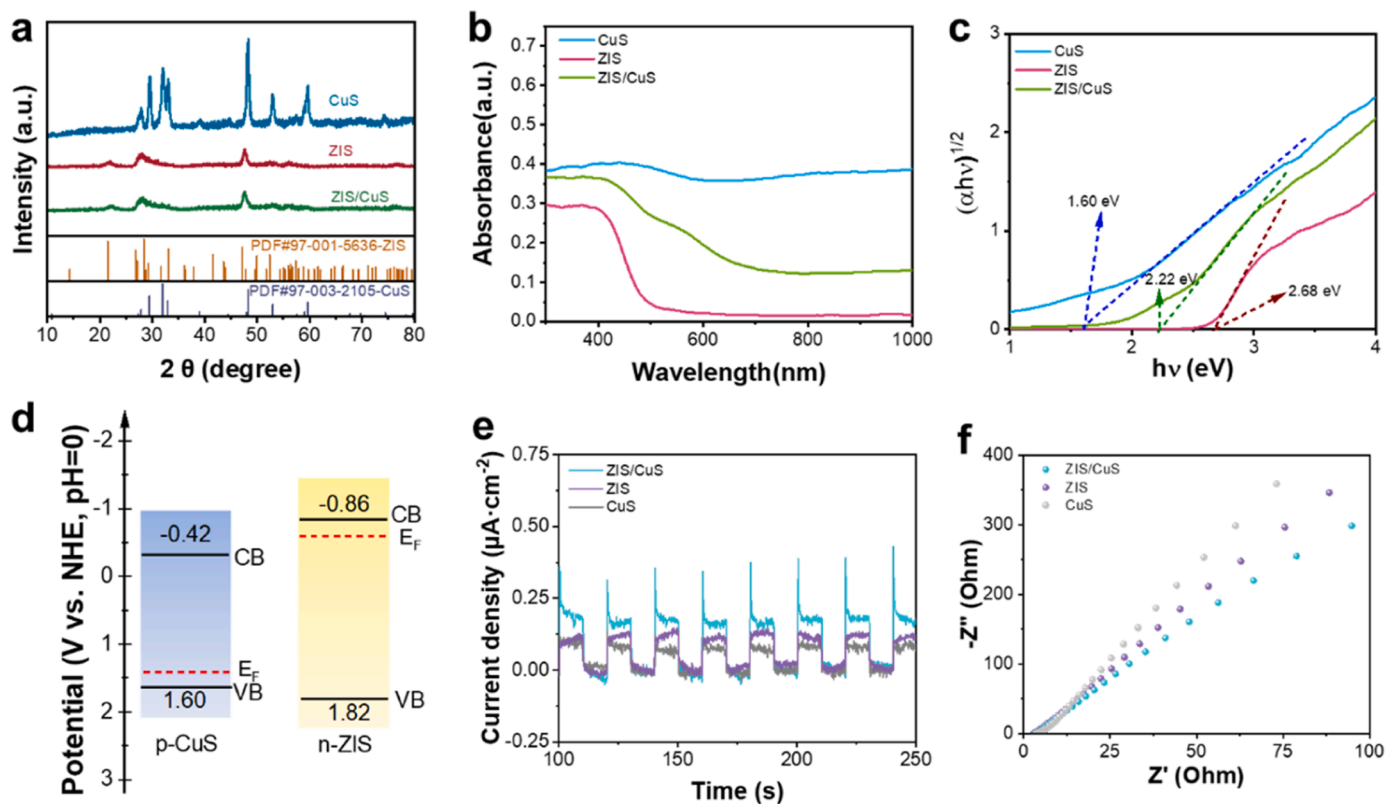


Fig. 2. (a) XRD patterns of ZIS, CuS, and ZIS/CuS. (b) UV-vis diffuse reflectance spectra of ZIS, CuS, and ZIS/CuS. (c) The Kubelka-Munk function is used to calculate the width and the corresponding light energy diagram to estimate the band gap of ZIS, CuS, and ZIS/CuS. (d) Energy level diagram of n-ZIS and p-CuS. (e) The photocurrent response of ZIS/CuS, ZIS, and CuS was measured using an electrochemical workstation (0.5 V vs. Ag/AgCl) under visible light irradiation ($\lambda > 420$ nm) and the light switching period was the 20 s (f) The Nyquist spectra of ZIS, CuS, and ZIS/CuS.

used as a seed by the in-situ growth of the ZIS nanoparticles. However, the typical nanosheets of ZIS were prepared without the addition of the CuS seed in Fig. S2b, as comparisons. Fig. 1a shows a field-emission scanning electron microscope (FESEM) image of ZIS/CuS, which

exhibits a distinctive four-cornered flower cage shape, named gemstone nanoflower. The representative high-resolution TEM (HRTEM) image of ZIS/CuS, as shown in Fig. 2b gave the presence of ZIS and CuS phases. The lattice spacings of the different 0.32 nm and 0.30 nm responded to

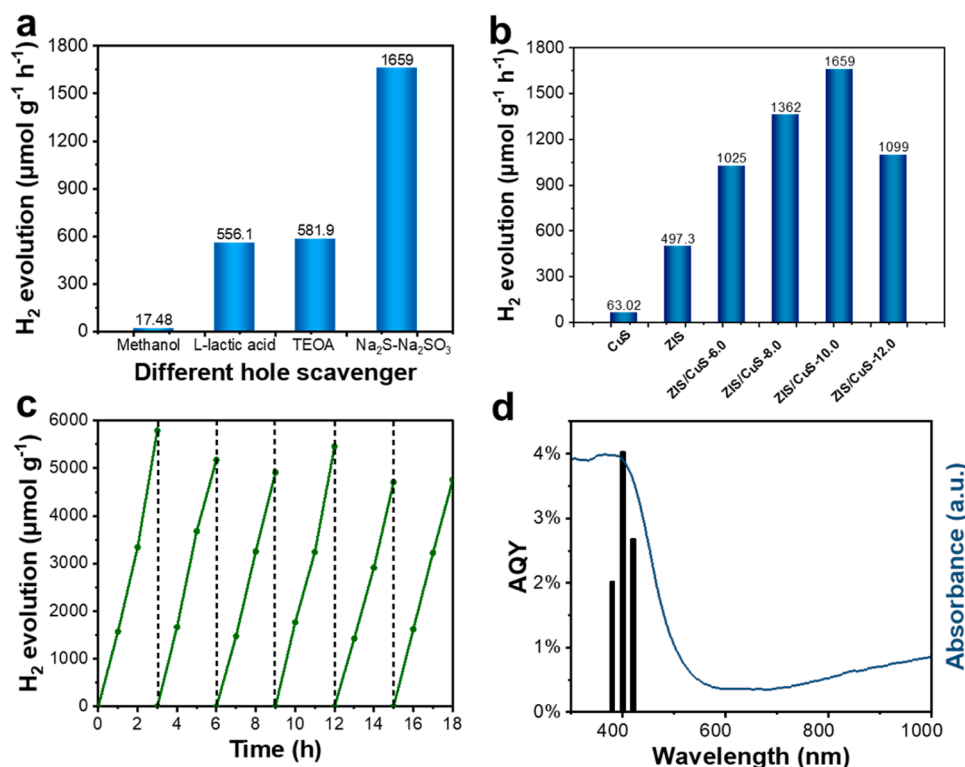


Fig. 3. (a) The relationship between the photocatalytic activity of ZIS/CuS and different hole sacrificial agents under visible light irradiation ($\lambda > 420$ nm). (b) Comparison of the hydrogen-producing activity of ZIS/CuS in Na₂S-Na₂SO₃ solution as a sacrificial agent in the photocatalytic system. The amount of the H₂ evolution of ZIS/CuS varies with the change in the amount of the precursor. (c) The cycle stability test of ZIS/CuS. (d) The wavelength dependence of AQY for ZIS/CuS. The absorption spectrum of ZIS/CuS is shown as a light blue line.

the ZIS (104) and CuS (102) planes, respectively, as displayed on the right in Fig. 1b. Furthermore, the EDX element mapping in Fig. 1c shows that CuS was covered by the ZIS to form a four-cornered flower cage (gemstone nanoflower). The uniformed distributions of each element in the ZIS/CuS (Fig. 1d-g) reflected that ZIS was mainly distributed on the surface of CuS.

3.2. Photoelectrochemical (PEC) and material properties

The X-ray diffraction (XRD) pattern of ZIS/CuS is shown in Fig. 2a. Compared with pristine CuS and ZIS, we could observe the features of diffraction peaks of ZIS. However, the peaks of CuS were not identified, which might be attributed to the low-weight contents of the CuS in ZIS/CuS. The weight ratio of Cu:Zn:In was determined to be 6.07:20.2:43.6 via inductively coupled plasma optical emission spectroscopy (ICP-OES). The UV-visible diffusion reflection spectra (UV-vis DRS) of the obtained samples are displayed in Fig. 2b. Typically, the ZIS shows the visible light-responsive photocatalyst. The CuS has broad strong absorption in the visible-near infrared region. As for ZIS/CuS, the two features of CuS and ZIS were composed. The band structures of the original ZIS and CuS were determined by UV-vis DRS spectra and Mott-Schottky curves at different frequencies [51]. The bandgap diagrams of all prepared samples were calculated as obtained by the following Kubelka-Munk equation:

$$\alpha h\nu = A (h\nu - E_g)^{n/2} \quad (3)$$

In the equation, α , h , and ν represent the absorption coefficient, Planck's constant, optical frequency, A is the constant and E_g is the bandgap energy, respectively. The value of exponential n is determined by the band gap type of the sample (direct band gap $n = 1$, indirect band gap $n = 4$). The E_g values of pure ZIS, CuS, and ZIS/CuS are determined to be about 2.68 [4], 2.02 [52], and 2.22 eV, respectively (Fig. 2c),

which were consistent with the reported literature [52]. From the Mott-Schottky plots results shown in Fig. S3, the flat potentials of ZIS and CuS relative to Ag/AgCl electrodes are -1.26 and 0.80 eV, and the positive slope of ZIS is typical of n-type semiconductors, while the p-type semiconductor characteristics of CuS with typical negative slopes are also well displayed, respectively. The distance between the conduction band (CB) of the n-type semiconductor material and the flat potential is about $0.1 \sim 0.2$ eV [53,54]. Therefore, the conduction band (CB) position of ZIS relative to the normal hydrogen electrode (NHE, pH = 0) is measured to be -0.86 eV. As for CuS with the p-type character, the band value of the valence band (VB) was 1.60 eV. Thus, the band diagrams of the ZIS and CuS are shown in Fig. 2d.

To evaluate the photoinduced charge separation and electrochemical properties of ZIS/CuS, we did the transient photocurrent and electrochemical impedance spectroscopy (EIS) measurements under visible light irradiation ($\lambda > 420$ nm). As shown in Fig. 2e, the ZIS/CuS exhibited a remarkable photocurrent density of $0.42 \mu\text{A cm}^{-2}$, which was 5.25 and 3.23 times higher than that of CuS ($0.08 \mu\text{A cm}^{-2}$) and ZIS ($0.13 \mu\text{A cm}^{-2}$), respectively, indicating efficient photogenerated charge separation. In addition, the EIS measurements revealed the interface properties between the electrode and the electrolyte. It is well known that frequency high-frequency semicircles in Nyquist diagrams can illustrate charge transfer processes. As shown in Fig. 2f, ZIS/CuS has the lowest charge-transfer resistance, so its arc is the smallest. These photoelectrochemical properties indicated that the ZIS/CuS could promote the separation and migration of the photoinduced electrons and holes.

3.3. Photocatalytic activity of HER

We investigated the photocatalytic activity and stability of ZIS/CuS for photocatalytic HER under visible light irradiation. The photocatalytic activity of ZIS/CuS in HER varies with different hole sacrificial agents in Fig. 3a. When the Na₂S-Na₂SO₃ solution was used as the

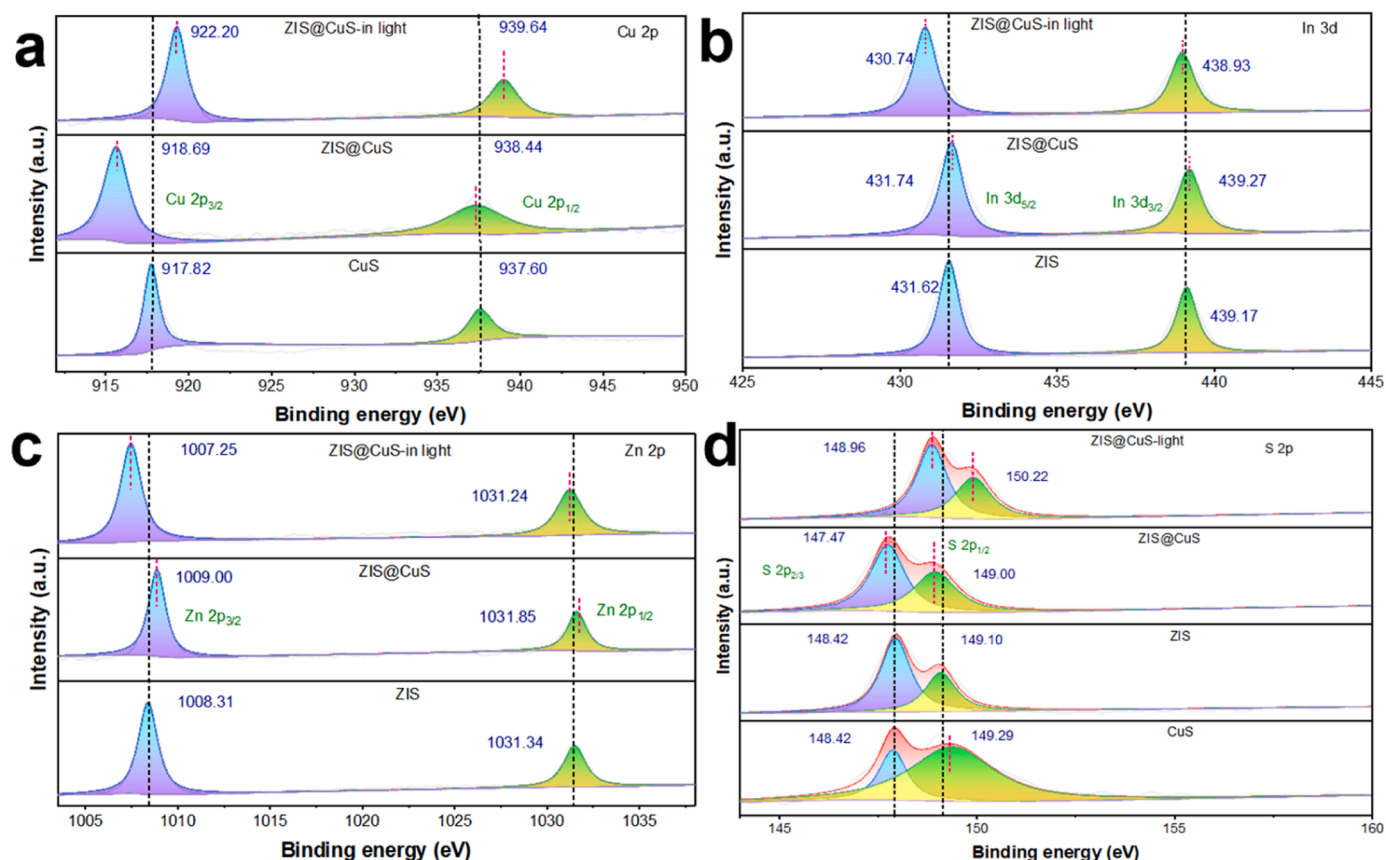


Fig. 4. High-resolution in-situ and ex-situ XPS spectra of (a) Cu 2p, (b) In 3d, (c) Zn 2p, and (d) S 2p levels of ZIS, CuS, and ZIS/CuS, respectively.

sacrificial agent, the hydrogen evolution reaction of ZIS/CuS showed the highest photocatalytic activity. Then low photocatalytic activity was given by the lactic acid and TEOA (triethanolamine) while using the methanol had the lowest catalytic activity. Thus, we used the $\text{NaSO}_3\text{-Na}_2\text{S}$ solution as a hole scavenger to investigate the photocatalytic activity in HER. With the increase of using the amount of CuS, the photocatalytic activity of ZIS/CuS in HER also increased, as shown in Fig. 3b. The photocatalytic hydrogen HER rate of ZIS/CuS (10 mg) was $1659 \mu\text{mol h}^{-1} \text{g}^{-1}$, its activity was better than that of the original CuS at HER rate of $63.02 \mu\text{mol h}^{-1} \text{g}^{-1}$ (26.3 times higher) and pure ZIS at HER rate of $497.3 \mu\text{mol h}^{-1} \text{g}^{-1}$ (3.34 times higher), respectively. It is attributed to the strong interaction between ZIS and CuS which forms a unique ZIS/CuS heterojunction. When increasing the amount of CuS seed to 12 mg, the HER rate of ZIS/CuS-12.0 was $1099 \mu\text{mol h}^{-1} \text{g}^{-1}$, which might be due to the excessive CuS hindering the light absorption of ZIS. Moreover, as displayed in Fig. S4 and Table S3, the nitrogen adsorption-desorption isotherm and pore size distribution curve show that ZIS/CuS has a high specific surface area and unique mesoporous properties, which are favorable for its high photocatalytic activity in HER. Furthermore, the stability of the sample is one of the important factors determine determining the photocatalytic activity. Fig. 3c shows six consecutive reactions of ZIS/CuS in HER. The photocatalytic activity of HER maintained good stability after 6 cycles of light irradiation for a long time and the slight fluctuation could be attributed to the testing errors or the consumption of sacrificial agents. After reactions, there were no significant changes in the XRD pattern and FESEM image of ZIS/CuS, as shown in Fig. S5 and Fig. S6, respectively. As shown in Fig. 3d, the apparent quantum yield (AQY) of ZIS/CuS is about 4.0% at 420 nm. This is a relatively high efficiency compared to previous reports as listed in Tables S1 and S2. The low AQY value at 380 nm is suggested to be due to the phototoxicity of the sulfide itself. These results suggested that the ZIS/CuS exhibited excellent photocatalytic activity of HER and stability.

3.4. In-situ XPS analysis

In-situ and ex-situ X-ray photoelectron spectroscopy (XPS) tests were performed on the samples to investigate the reason why ZIS/CuS showed high photocatalytic activity in HER [55]. The surface compositions and corresponding electronic states of different elements in ZIS/CuS were performed. In addition, the direction of electron transfer can be judged by the change of XPS binding energy, which helps to further analyze the charge transfer type of heterojunction. The full XPS spectral analysis of ZIS/CuS showed each element's characteristic peaks of CuS and ZIS (Fig. S7), indicating that the heterojunction was formed by the combination of CuS and ZIS. Fig. 4a shows a high-resolution Cu 2p spectrum of ZIS/CuS, in which two binding energy peaks of Cu $2p_{1/2}$ and Cu $2p_{3/2}$ at 938.44 eV and 918.69 eV respectively, can be observed. Due to the different electron densities of the Cu element, the reduction of the Cu binding energy in ZIS/CuS was gotten to a lower position compared to that of the pristine CuS. Similarly, the S 2p of ZIS/CuS also showed a peak shift to the lower binding energy (Fig. 4d). Meanwhile, as shown in Fig. 4b and 4c, the two binding energy peaks of In 3d orbitals of the $3d_{3/2}$ (439.27 eV) and $3d_{5/2}$ (431.74 eV) and Zn $2p_{1/2}$ (1031.85 eV) and Zn $2p_{3/2}$ (1009.00 eV) were observed in ZIS/CuS, respectively. Compared with the pristine ZIS, the binding energy peaks of both Zn 2p and In 3d in ZIS/CuS were shifted to higher positions. The ex-situ XPS results show that the binding energies of In and Zn in ZIS/CuS shift towards higher directions, indicating that ZIS components could be considered electron donors, while Cu components moved in a lower direction, indicating that CuS components could be considered as electron acceptors. This indicated that electrons could migrate from ZIS to CuS in the dark, to form a strong built-in electric field focusing (IEF) heterojunction.

In addition, we designed the in-situ XPS experiment to prove the photoinduced carriers transfer route of the ZIS/CuS. As shown in Fig. 4, the in-situ XPS results of the ZIS/CuS-light showed that the binding

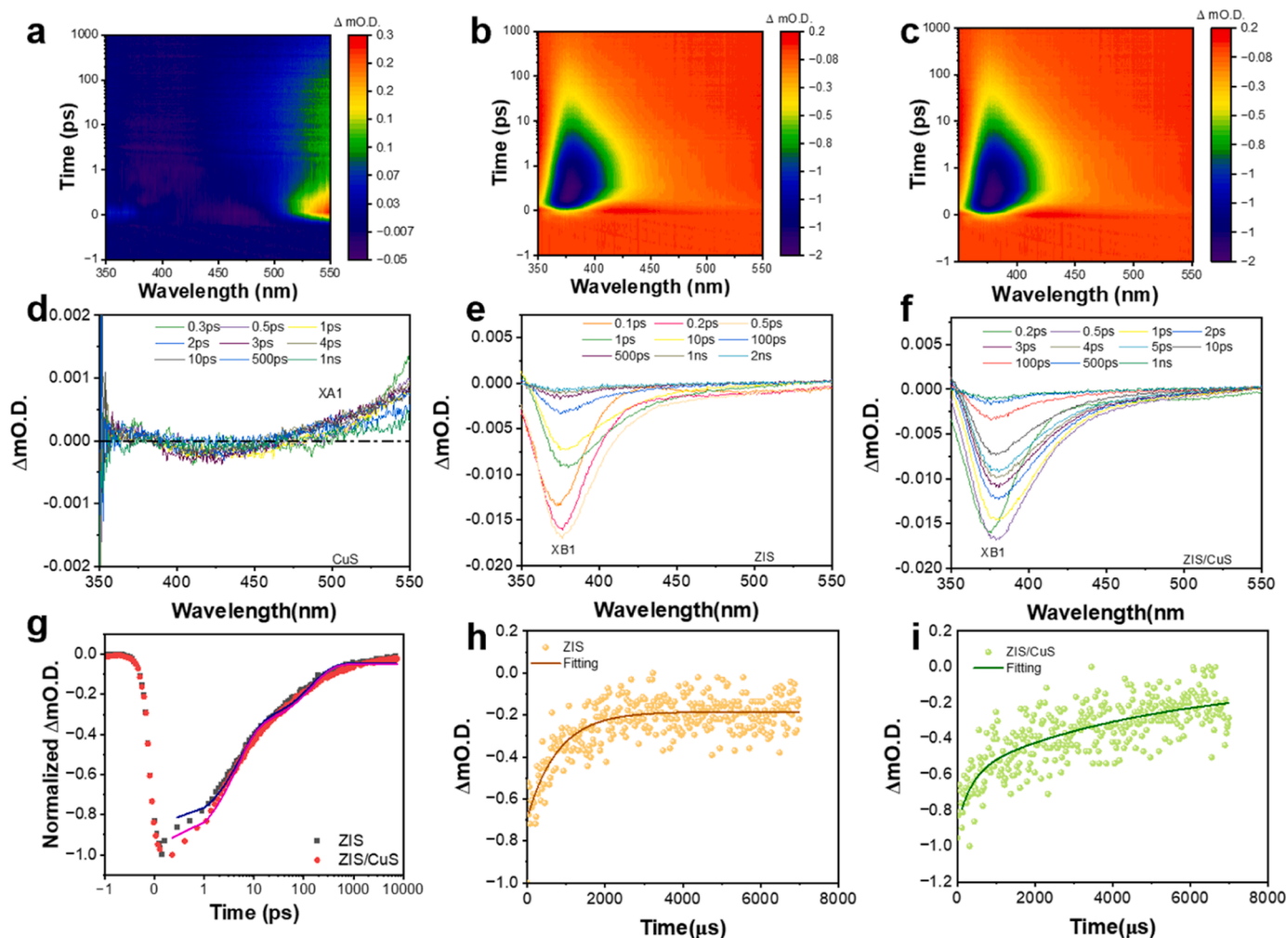


Fig. 5. Time-resolved transient absorption spectra of (a, d) CuS, (b, e) ZIS, (c, f) ZIS/CuS upon 300-nm laser excitation. (g) Kinetic profiles ZIS/CuS and ZIS at femtosecond to nanosecond probing at 380 nm. Best fitting lines were in blue and purple. (h, i) Kinetic profiles at the microsecond region of ZIS and ZIS/CuS upon 355-nm laser excitation, probing at 380 nm.

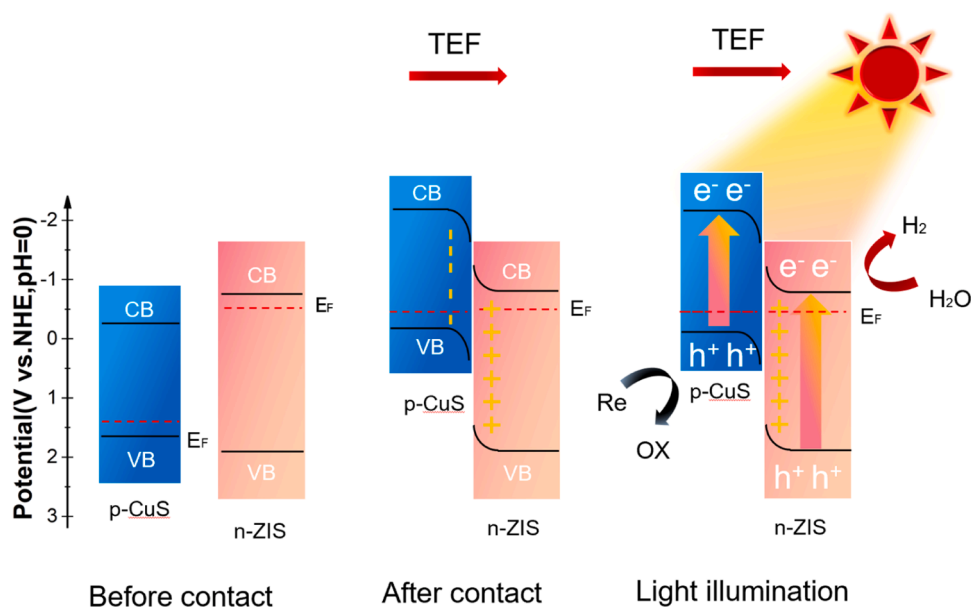


Fig. 6. The p-n heterojunction formation under visible light irradiation, and schematic diagram of the photoinduced electron transfer mechanism with type-II scheme.

energies of Zn and In in ZIS/CuS-light moved towards lower binding energies and those of Cu and S move towards higher binding energies under visible light irradiation. It shows the different situations of the binding energy of Cu, Zn, In, and S in ZIS/CuS, when illuminated by visible light, they both move in opposite directions, indicating that photogenerated electrons can be transferred from CuS to ZIS. The barrier between CuS and ZIS could hinder the photoinduced carrier transfer from the ZIS to CuS. So far, these XPS results provide important support for our proposed mechanism of photogenerated carrier transfer with type-II scheme for ZIS/CuS heterojunctions.

3.5. Dynamic analysis of photoinduced carrier

To elucidate the photoinduced carrier dynamics of ZIS/CuS with high photocatalytic activity in HER, we performed femtosecond (fs) time-resolved transient absorption (TAS) measurements using the pump-probe technique under 300 nm laser excitation. The TAS of CuS, ZIS, and ZIS/CuS are shown in Fig. 5a-c, respectively. We could observe the exciton photo-bleaching XB1 at 380 nm through the state filling in ZIS, as shown in Fig. 5b and 5e. As displayed in Fig. 5a and 5d, the only small change at around 410 nm of photo-bleaching signal and broad photo-absorption signal at large 500 nm (XA1) of CuS observed. As for ZIS/CuS in Figs. 5c and 5f, the photo-bleaching peak of XB1 at 380 nm appeared in ZIS/CuS, indicating that the bleaching signal mainly belonged to the ZIS phase. The XB1 peak in ZIS/CuS exhibited a slower recovery than that of ZIS, indicating that the photoinduced electron transferred from CuS to ZIS, prolonging the lifetime of free carriers. Therefore, the heterojunction photocatalysts could promote the separation of photogenerated electron-hole pairs. Fig. 5g gives the kinetic profiles of ZIS and ZIS/CuS probing at 380 nm. The bi-exponential function curves of the dynamic trajectories of photoexcited bleaching and recovery were fitted (as shown in Table S4), and the time constants of ZIS/CuS were estimated to be 4.34 ps (τ_1) and 144 ps (τ_2), respectively. The low component of ZIS/CuS was a little longer than that of ZIS, suggesting the efficient charge separation favoring the high performance of photocatalytic HER. Since the time window at fs-nanosecond (ns) didn't determine the lifetime of ZIS/CuS, we did the nanosecond to millisecond photolysis spectroscopy measurements. We selected 355 nm to excite the ZIS and ZIS/CuS to monitor the photoinduced carrier lifetime. As shown in Fig. 5h and 5i, the kinetic profiles of the ZIS/CuS indicated that the lifetime of ZIS/CuS could reach 4.89 ms, as shown in Table S5, which was ultralong lifetime compared with general nanoparticles with only ns lifetime [56] and 6 times higher than that of ZIS (796 μ s), suggesting that the extraordinarily long lifetime favored the high photocatalytic HER.

3.6. Mechanism for the photocatalytic HER

From the above results, we proposed the type-II mechanism in ZIS/CuS for photocatalytic HER, as displayed in Fig. 6. Firstly, when p-CuS and n-ZIS contacted each other, the Fermi level reached the equilibrium through the electron transfer from the ZIS to CuS forming the heterojunctions with the strong IEF, favoring photogenerated charge separation. The depletion layers at the interfaces with band bending between ZIS and CuS could be formed. It favored the photoinduced interfacial charge transfer. Under visible light irradiation, both ZIS and CuS could be excited to produce electrons and holes. The electron and hole could be easily transferred from the CuS to ZIS and ZIS to CuS, respectively, due to the band bending of the barrier preventing the charge carriers from moving in the opposite direction, forming the type-II mechanism. The electrons on the CB of ZIS were used for water splitting to produce H_2 . While the holes on the VB of CuS were consumed by the sacrificial agents. Thus, the spatial separation of the photoinduced electrons and holes with type-II heterojunctions in ZIS/CuS is attributed to the high performance of photocatalytic HER.

4. Conclusion

In summary, the gemstone nanoflower-shaped ZIS/CuS heterostructures have been successfully synthesized. The ZIS/CuS exhibited high activity and stability for photocatalytic HER. It was attributed to the efficient photogenerated charge separation forming the type-II mechanism and ultralong lifetime of 4.89 ms, which were demonstrated by the in-situ XPS and fs-ms TA measurements. The strong IEF prevented the photoinduced carrier transfer reversely, favoring the high performance of photocatalytic H_2 production. This provides a new pathway through the novel structure of p-n heterojunctions for type-II mechanism in particulate photocatalyst systems.

CRediT authorship contribution statement

Luan Xue: Investigation, Formal analysis. **Yu Ziqi:** Writing – review & editing, Writing – original draft, Investigation, Formal analysis, Data curation. **Lian Zichao:** Writing – review & editing, Writing – original draft, Validation, Supervision, Project administration, Investigation, Funding acquisition, Formal analysis, Conceptualization. **Yang Yupeng:** Formal analysis, Data curation. **Xiao Han:** Writing – review & editing, Investigation, Formal analysis, Data curation. **Zi Jiangzhi:** Writing – review & editing, Investigation, Formal analysis, Data curation. **Luo Di:** Validation, Investigation, Data curation.

Declaration of Competing Interest

The authors declare that they have no known competing financial interests or personal relationships that could have appeared to influence the work reported in this paper.

Data availability

Data will be made available on request.

Acknowledgements

This work was supported by the National Natural Science Foundation of China (22109097).

Appendix A. Supporting information

Supplementary data associated with this article can be found in the online version at doi:10.1016/j.apcatb.2024.123702.

References

- [1] Z. Lian, Y. Kobayashi, J.J.M. Vequizo, C.S.K. Ranasinghe, A. Yamakata, T. Nagai, K. Kimoto, K. Kobayashi, K. Tanaka, T. Teranishi, M. Sakamoto, Harnessing infrared solar energy with plasmonic energy upconversion, *Nat. Sustain.* 5 (2022) 1092–1099.
- [2] Z. Lian, F. Wu, J. Zi, G. Li, W. Wang, H. Li, Infrared light-induced anomalous defect-mediated plasmonic hot electron transfer for enhanced photocatalytic hydrogen evolution, *J. Am. Chem. Soc.* 145 (2023) 15482–15487.
- [3] Z. Lian, M. Sakamoto, J.J.M. Vequizo, C.S.K. Ranasinghe, A. Yamakata, T. Nagai, K. Kimoto, Y. Kobayashi, N. Tamai, T. Teranishi, Plasmonic p-n junction for infrared light to chemical energy conversion, *J. Am. Chem. Soc.* 141 (2019) 2446–2450.
- [4] Y. Zhong, M. Li, X. Luan, F. Gao, H. Wu, J. Zi, Z. Lian, Ultrathin $ZnIn_2S_4/ZnSe$ heteronanoshells with modulated S-scheme enable high efficiency of visible-light-responsive photocatalytic hydrogen evolution, *Appl. Catal. B: Environ.* 335 (2023) 122859.
- [5] X. Luan, Z. Yu, J. Zi, F. Gao, Z. Lian, Photogenerated defect-transit dual S-scheme charge separation for highly efficient hydrogen production, *Adv. Funct. Mater.* 33 (2023) 2304259.
- [6] Z. Li, J. Zi, X. Luan, Y. Zhong, M. Qu, Y. Wang, Z. Lian, Localized surface plasmon resonance promotes metal-organic framework-based photocatalytic hydrogen evolution, *Adv. Funct. Mater.* 33 (2023) 2303069.
- [7] F. Gao, H. Xiao, J. Yang, X. Luan, D. Fang, L. Yang, J. Zi, Z. Lian, Modulation of electronic density in ultrathin g-C₃N₄ for enhanced photocatalytic hydrogen evolution through an efficient hydrogen spillover pathway, *Appl. Catal. B: Environ.* 341 (2024) 123334.

- [8] Q. Wang, T. Hisatomi, Q. Jia, H. Tokudome, M. Zhong, C. Wang, Z. Pan, T. Takata, M. Nakabayashi, N. Shibata, Y. Li, I.D. Sharp, A. Kudo, T. Yamada, K. Domen, Scalable water splitting on particulate photocatalyst sheets with a solar-to-hydrogen energy conversion efficiency exceeding 1%, *Nat. Mater.* 15 (2016) 611–615.
- [9] J. Low, J. Yu, M. Jaroniec, S. Wageh, A.A. Al-Ghamdi, Heterojunction photocatalysts, *Adv. Mater.* 29 (2017) 1601694.
- [10] L. Jiang, H. Yu, L. Shi, Y. Zhao, Z. Wang, M. Zhang, S. Yuan, Optical band structure and photogenerated carriers transfer dynamics in FTO/TiO₂ heterojunction photocatalysts, *Appl. Catal. B* 199 (2016) 224–229.
- [11] X. Liu, Y. Zhao, X. Yang, Q. Liu, X. Yu, Y. Li, H. Tang, T. Zhang, Porous Ni₅P₄ as a promising cocatalyst for boosting the photocatalytic hydrogen evolution reaction performance, *Appl. Catal. B* 275 (2020) 119144.
- [12] K. Chang, H. Pang, X. Hai, G. Zhao, H. Zhang, L. Shi, F. Ichihara, J. Ye, Ultra-small freestanding amorphous molybdenum sulfide colloidal nanodots for highly efficient photocatalytic hydrogen evolution reaction, *Appl. Catal., B* 232 (2018) 446–453.
- [13] P. Zhang, T. Wang, X. Chang, J. Gong, Effective charge carrier utilization in photocatalytic conversions, *Acc. Chem. Res.* 49 (2016) 911–921.
- [14] W. Li, A. Elzatahry, D. Aldhayan, D. Zhao, Core-shell structured titanium dioxide nanomaterials for solar energy utilization, *Chem. Soc. Rev.* 47 (2018) 8203–8237.
- [15] Q. Xu, L. Zhang, B. Cheng, J. Fan, J. Yu, S-Scheme heterojunction photocatalyst, *Chem* 6 (2020) 1543–1559.
- [16] X. Zhang, J. Xiao, M. Hou, Y. Xiang, H. Chen, Robust visible/near-infrared light driven hydrogen generation over Z-scheme conjugated polymer/CdS hybrid, *Appl. Catal. B* 224 (2018) 871–876.
- [17] X. Yue, S. Yi, R. Wang, Z. Zhang, S. Qiu, Well-controlled SrTiO₃@Mo₂C core-shell nanofiber photocatalyst: boosted photo-generated charge carriers transportation and enhanced catalytic performance for water reduction, *Nano Energy* 47 (2018) 463–473.
- [18] Q. Xu, B. Zhu, B. Cheng, J. Yu, M. Zhou, W. Ho, Photocatalytic H₂ evolution on graphdiyne/g-C₃N₄ hybrid nanocomposites, *Appl. Catal., B* 255 (2019) 117770.
- [19] Q. Xu, B. Cheng, J. Yu, G. Liu, Making co-condensed amorphous carbon/g-C₃N₄ composites with improved visible-light photocatalytic H₂-production performance using Pt as cocatalyst, *Carbon* 118 (2017) 241–249.
- [20] M.F. Kuehnle, E. Reisner, Solar hydrogen generation from lignocellulose, *Angew. Chem. Int. Ed.* 57 (2018) 3290–3296.
- [21] J. Jia, L.C. Seitz, J.D. Benck, Y. Huo, Y. Chen, J.W.D. Ng, T. Bilir, J.S. Harris, T. F. Jaramillo, Solar water splitting by photovoltaic-electrolysis with a solar-to-hydrogen efficiency over 30%, *Nat. Commun.* 7 (2016) 13237.
- [22] X. Ji, H. Xu, S. Liang, L. Gan, R. Zhang, X. Wang, 3D ordered macroporous Pt/ZnS@ZnO core-shell heterostructure for highly effective photocatalytic hydrogen evolution, *Int. J. Hydrogen Energy* 47 (2022) 17640–17649.
- [23] X. Wang, Q. Li, H. Xu, L. Gan, X. Ji, H. Liu, R. Zhang, CuS-modified ZnO rod/reduced graphene oxide/CdS heterostructure for efficient visible-light photocatalytic hydrogen generation, *Int. J. Hydrogen Energy* 45 (2020) 28394–28403.
- [24] Y. Zhu, J. Li, C.-L. Dong, J. Ren, Y.-C. Huang, D. Zhao, R. Cai, D. Wei, X. Yang, C. Lv, W. Theis, Y. Bu, W. Han, S. Shen, D. Yang, Red phosphorus decorated and doped TiO₂ nanofibers for efficient photocatalytic hydrogen evolution from pure water, *Appl. Catal. B* 255 (2019) 117764.
- [25] M.H. Basha, N.O. Gopal, Solution combustion synthesis and characterization of phosphorus doped TiO₂-CeO₂ nanocomposite for photocatalytic applications, *Mater. Sci. Eng. B* 236–237 (2018) 43–47.
- [26] R. Sathre, J.B. Greenblatt, K. Walczak, I.D. Sharp, J.C. Stevens, J.W. Ager, F. A. Houle, Opportunities to improve the net energy performance of photoelectrochemical water-splitting technology, *Energy Environ. Sci.* 9 (2016) 803–819.
- [27] J. Pan, Y. Fu, G. Xiao, J. Niu, J. Cao, J. Wang, Y. Zheng, C. Li, Photocatalytic overall water splitting hydrogen evolution enhancement of ZnO nanoarrays/LaCrO₃ film heterojunction via HER/OER synergism of CoP/FTO, *J. Environ. Chem. Eng.* 10 (2022) 108587.
- [28] J. Yi, H. Li, Y. Gong, X. She, Y. Song, Y. Xu, J. Deng, S. Yuan, H. Xu, H. Li, Phase and interlayer effect of transition metal dichalcogenide cocatalyst toward photocatalytic hydrogen evolution: the case of MoSe₂, *Appl. Catal. B* 243 (2019) 330–336.
- [29] L. Chen, Y. Xu, Z. Yang, K. Zhang, B. Chen, Cobalt (II)-based open-framework systems constructed on g-C₃N₄ for extraordinary enhancing photocatalytic hydrogen evolution, *Appl. Catal. B* 277 (2020) 119207.
- [30] X. Peng, L. Ye, Y. Ding, L. Yi, C. Zhang, Z. Wen, Nanohybrid photocatalysts with ZnIn₂S₄ nanosheets encapsulated UiO-66 octahedral nanoparticles for visible-light-driven hydrogen generation, *Appl. Catal. B* 260 (2020) 118152.
- [31] F. Zhou, Y. Zhang, J. Wu, W. Yang, X. Fang, T. Jia, Y. Ling, P. He, Q. Liu, J. Lin, Utilizing Er-doped ZnIn₂S₄ for efficient photocatalytic CO₂ conversion, *Appl. Catal. B* 341 (2024) 123347.
- [32] G. Zuo, Y. Wang, W.L. Teo, A. Xie, Y. Guo, Y. Dai, W. Zhou, D. Jana, Q. Xian, W. Dong, Y. Zhao, Ultrathin ZnIn₂S₄ nanosheets anchored on Ti₃C₂TX MXene for photocatalytic H₂ evolution, *Angew. Chem. Int. Ed.* 59 (2020) 11287–11292.
- [33] S. Wang, B.Y. Guan, X. Wang, X.W.D. Lou, Formation of hierarchical Co₉S₈@ZnIn₂S₄ heterostructured cages as an efficient photocatalyst for hydrogen evolution, *J. Am. Chem. Soc.* 140 (2018) 15145–15148.
- [34] D. Ao, J. Zhang, H. Liu, Visible-light-driven photocatalytic degradation of pollutants over Cu-doped NH₂-MIL-125(Ti), *J. Photochem. Photobiol. A* 364 (2018) 524–533.
- [35] X. Sun, X. Luo, S. Jin, X. Zhang, H. Wang, W. Shao, X. Wu, Y. Xie, Surface modification of ZnIn₂S₄ layers to realize energy-transfer-mediated photocatalysis, *Natl. Sci. Rev.* 9 (2022).
- [36] H. Liu, J. Zhang, D. Ao, Construction of heterostructured ZnIn₂S₄@NH₂-MIL-125 (Ti) nanocomposites for visible-light-driven H₂ production, *Appl. Catal. B* 221 (2018) 433–442.
- [37] Y. Zhu, L. Wang, Y. Liu, L. Shao, X. Xia, In-situ hydrogenation engineering of ZnIn₂S₄ for promoted visible-light water splitting, *Appl. Catal. B* 241 (2019) 483–490.
- [38] Z. Zhang, L. Huang, J. Zhang, F. Wang, Y. Xie, X. Shang, Y. Gu, H. Zhao, X. Wang, In situ constructing interfacial contact MoS₂/ZnIn₂S₄ heterostructure for enhancing solar photocatalytic hydrogen evolution, *Appl. Catal. B* 233 (2018) 112–119.
- [39] K. Singh, J. Nowotny, V. Thangadurai, Amphoteric oxide semiconductors for energy conversion devices: a tutorial review, *Chem. Soc. Rev.* 42 (2013) 1961–1972.
- [40] N. Li, W. Fu, C. Chen, M. Liu, F. Xue, Q. Shen, J. Zhou, Controlling the core-shell structure of CuS@CdS heterojunction via seeded growth with tunable photocatalytic activity, *ACS Sustain. Chem.* 6 (2018) 15867–15875.
- [41] J.Y. Do, R.K. Chava, S.K. Kim, K. Nahm, N.-K. Park, J.-P. Hong, S.J. Lee, M. Kang, Fabrication of core@interface:shell structured CuS@CuInS₂/In₂S₃ particles for highly efficient solar hydrogen production, *Appl. Surf. Sci.* 451 (2018) 86–98.
- [42] C. Mondal, A. Singh, R. Sahoo, A.K. Sasmal, Y. Negishi, T. Pal, Preformed ZnS nanoflower prompted evolution of CuS/ZnS p-n heterojunctions for exceptional visible-light driven photocatalytic activity, *N. J. Chem.* 39 (2015) 5628–5635.
- [43] X. Xu, Z. Gao, Z. Cui, Y. Liang, Z. Li, S. Zhu, X. Yang, J. Ma, Synthesis of Cu₂O octadecahedron/TiO₂ quantum dot heterojunctions with high visible light photocatalytic activity and high stability, *ACS Appl. Mater.* 8 (2016) 91–101.
- [44] Z. Lian, M. Sakamoto, J.J.M. Vequizo, C.S.K. Ranasinghe, A. Yamakata, T. Nagai, K. Kimoto, Y. Kobayashi, N. Tamai, T. Teranishi, Plasmonic p-n junction for infrared light to chemical energy conversion, *J. Am. Chem. Soc.* 141 (2019) 2446–2450.
- [45] X. Du, J. Hu, J. Xie, A. Hao, Z. Lu, Y. Cao, Simultaneously tailor band structure and accelerate charge separation by constructing novel In(OH)₃-TiO₂ heterojunction for enhanced photocatalytic water reduction, *Appl. Surf. Sci.* 593 (2022) 153305.
- [46] Y.-H. Li, M.-Y. Qi, J.-Y. Li, Z.-R. Tang, Y.-J. Xu, Noble metal free CdS@CuS-NixP hybrid with modulated charge transfer for enhanced photocatalytic performance, *Appl. Catal. B* 257 (2019) 117934.
- [47] J. Sun, X. Li, Q. Zhao, M.O. Tadé, S. Liu, Construction of p-n heterojunction β-Bi₂O₃/BiVO₄ nanocomposite with improved photoinduced charge transfer property and enhanced activity in degradation of ortho-dichlorobenzene, *Appl. Catal. B* 219 (2017) 259–268.
- [48] Y. Wang, M.K. Bayazit, S.J.A. Moniz, Q. Ruan, C.C. Lau, N. Martynovich, J. Tang, Linker-controlled polymeric photocatalyst for highly efficient hydrogen evolution from water, *Energy Environ. Sci.* 10 (2017) 1643–1651.
- [49] M.A. Khan, P. Varadhan, V. Ramalingam, H.-C. Fu, H. Idriss, J.-H. He, Importance of oxygen measurements during photoelectrochemical water-splitting reactions, *ACS Energy Lett.* 4 (2019) 2712–2718.
- [50] W. Xu, W. Gao, L. Meng, W. Tian, L. Li, Incorporation of sulfate anions and sulfur vacancies in ZnIn₂S₄ photoanode for enhanced photoelectrochemical water splitting, *Adv. Energy Mater.* 11 (2021) 2101181.
- [51] J.F. Guayquil-Sosa, B. Serrano-Rosales, P.J. Valadés-Pelayo, H. de Lasa, Photocatalytic hydrogen production using mesoporous TiO₂ doped with Pt, *Appl. Catal. B* 211 (2017) 337–348.
- [52] Y. Wang, M. Liu, C. Wu, J. Gao, M. Li, Z. Xing, Z. Li, W. Zhou, Hollow nanoboxes Cu_{2-x}S@ZnIn₂S₄ core-shell S-scheme heterojunction with broad-spectrum response and enhanced photothermal-photocatalytic performance, *Small* 18 (2022) 2202544.
- [53] G. Zuo, S. Ma, Z. Yin, W. Chen, Y. Wang, Q. Ji, Q. Xian, S. Yang, H. He, Z-scheme modulated charge transfer on InVO₄@ZnIn₂S₄ for durable overall water splitting, *Small* 19 (2023) 2207031.
- [54] Y. Zhong, J. Zi, F. Wu, Z. Li, X. Luan, F. Gao, Z. Lian, Defect-mediated electron transfer in Pt-CuInS₂/CdS heterostructured nanocrystals for enhanced photocatalytic H₂ evolution, *ACS Appl. Nano Mater.* 5 (2022) 7704–7713.
- [55] Q. Luan, X. Xue, R. Li, L. Gu, W. Dong, D. Zhou, X. Wang, B. Li, G. Wang, C. Hou, Boosting photocatalytic hydrogen evolution: orbital redistribution of ultrathin ZnIn₂S₄ nanosheets via atomic defects, *Appl. Catal. B* 305 (2022) 121007.
- [56] Z. Lian, M. Sakamoto, Y. Kobayashi, N. Tamai, J. Ma, T. Sakurai, S. Seki, T. Nakagawa, M.-W. Lai, M. Haruta, H. Kurata, T. Teranishi, Anomalous photoinduced hole transport in type I core/mesoporous-shell nanocrystals for efficient photocatalytic H₂ evolution, *ACS Nano* 13 (2019) 8356–8363.